

Physics-Informed Latent Neural Operator for Real-time Predictions of Complex Physical Systems

Sharmila Karumuri^a, Lori Graham-Brady^a, Somdatta Goswami^{a,*}

^aJohns Hopkins University, Department of Civil and Systems Engineering, Baltimore, 21218, Maryland, USA

Abstract

Deep operator network (DeepONet) has shown great promise as a surrogate model for systems governed by partial differential equations (PDEs), learning mappings between infinite-dimensional function spaces with high accuracy. However, achieving low generalization errors often requires highly overparameterized networks, posing significant challenges for large-scale, complex systems. To address these challenges, latent DeepONet [1, 2] was proposed, introducing a two-step approach: first, a reduced-order model is used to learn a low-dimensional latent space, followed by operator learning on this latent space. While effective, this method is inherently data-driven, relying on large datasets and making it difficult to incorporate governing physics into the framework. Additionally, the decoupled nature of these steps prevents end-to-end optimization and the ability to handle data scarcity. This work introduces PI-Latent-NO, a physics-informed latent operator learning framework that overcomes these limitations. Our architecture employs two coupled DeepONets in an end-to-end training scheme: the first, termed *Latent-DeepONet*, identifies and learns the low-dimensional latent space, while the second, *Reconstruction-DeepONet*, maps the latent representations back to the original physical space. By integrating governing physics directly into the training process, our approach requires significantly fewer data samples while achieving high accuracy. Furthermore, the framework is computationally and memory efficient, exhibiting nearly constant scaling behavior on a single GPU and demonstrating the potential for further efficiency gains with distributed training. We validate the proposed method on high-dimensional parametric PDEs, demonstrating its effectiveness as a proof of concept and its potential scalability for large-scale systems.

Keywords:

physics-informed neural operators, latent representations, partial differential equations

1. Introduction

Neural operators have emerged as a powerful class of deep learning models for building efficient surrogates for expensive parametric partial differential equations (PDEs). These operators can be categorized into meta-architectures, those based on the universal approximation theorem for operators [3] such as Deep Operator Networks (DeepONet) [4], resolution-

*Corresponding author

independent neural operator (RINO) [5], and basis-to-basis operator learning [6]; and those based on integral transforms, including the Graph Kernel Network (GKN) [7], Fourier Neural Operator (FNO) [8], Wavelet Neural Operator (WNO) [9], and Laplace Neural Operator (LNO) [10]. These models learn mappings between infinite-dimensional function spaces, accelerating complex simulations such as material failure prediction [11] and climate modeling [12], while also addressing tasks such as uncertainty propagation [13, 14, 15, 16], inverse problems (model calibration) [17, 18, 19, 20, 21, 22], and design optimization [23, 24] across diverse fields. However, their practical deployment faces three critical challenges: degrading performance with increasing system dimensionality and complexity, the requirement for extensive training data, and the inability to guarantee physics compliance in their predictions.

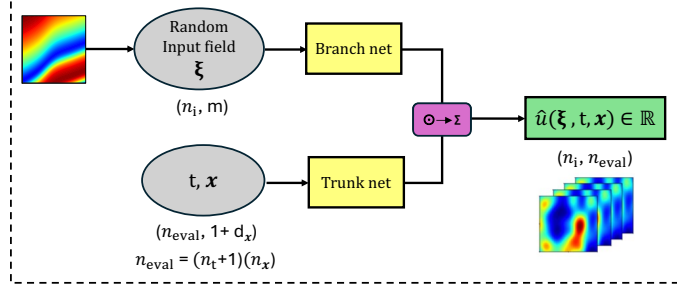
While recent advances in latent space operator learning and physics-informed training have separately addressed some of these limitations, a unified framework that simultaneously tackles all these challenges has remained elusive. Existing latent deep neural operators [1, 25, 2], though computationally efficient, rely on a two-step training process: first learning an efficient latent space through a reduced order model, then learning the neural operator within this latent space. This separation makes physics compliance difficult to achieve. Conversely, physics-informed variants often become computationally intractable for complex systems, primarily due to the prohibitively high computational cost associated with calculating PDE gradient terms. Recent advancements in separable techniques [26, 27] have made these frameworks more computationally efficient, yet they remain restricted to PDEs solvable using the separation of variables.

In this paper, we introduce the Physics-Informed Latent Neural Operator (see Figure 1b), representing a fundamental shift in approaching these challenges. Among the various neural operators developed, we employ DeepONet for its architectural flexibility. Our framework combines dimensionality reduction technique with physics-informed training through two coupled DeepONets trained in a single shot. The first network learns compact latent representations of the system dynamics, while the second reconstructs solutions in the original space. This architecture introduces built-in separability that enables approximately linear scaling with problem dimensionality—a significant advancement over existing methods that typically scale exponentially. Our key contributions include:

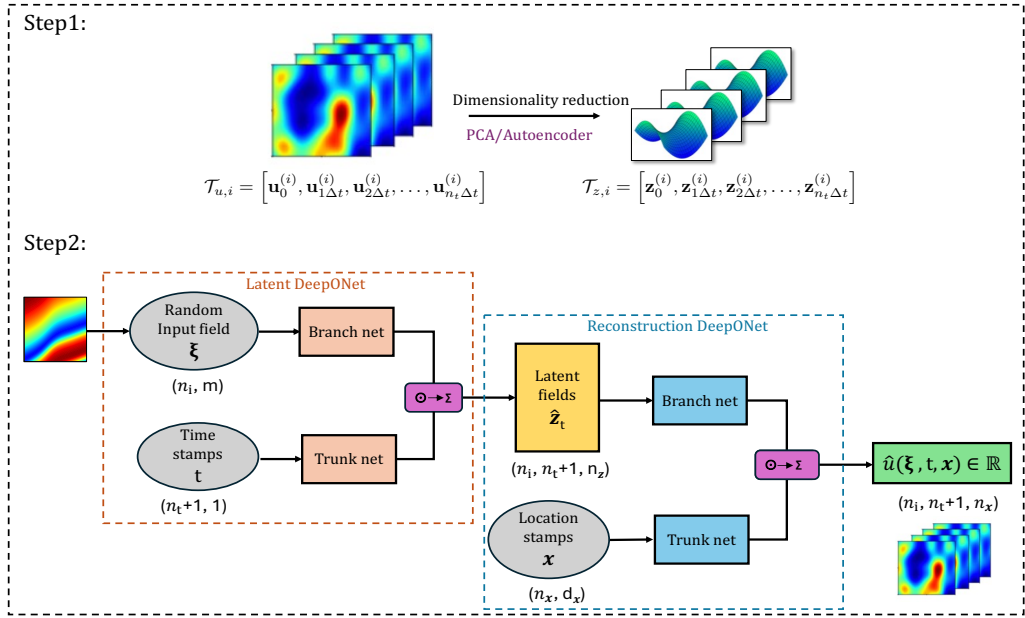
- The first end-to-end neural operator framework that performs learning directly in latent space, enabling efficient handling of high-dimensional problems by leveraging the governing physics alongside a small set of labeled data.
- The architecture with inherent separability that drastically accelerates training and inference for high-dimensional problems.
- Demonstration of approximately linear scaling with problem size, making our approach particularly valuable for complex, high-dimensional systems.

As a proof-of-concept, we demonstrate that our framework achieves state-of-the-art accuracy while requiring significantly fewer computational resources and training data compared to existing methods. These results suggest a promising direction for real-time prediction of complex physical systems, with potential applications ranging from climate modeling to engineering design optimization.

The remainder of this paper is structured as follows: Section 2 reviews recent advances in neural operators, latent neural operators, and reduced-order models. In Section 3, we



(a) Architecture of the Physics-Informed Vanilla Neural Operator (PI-Vanilla-NO). The branch network processes n_i input functions sampled at m sensor locations, while the trunk network handles $n_{\text{eval}} = (n_t+1) \times n_x$ spatiotemporal coordinates. The network outputs solution responses for all input functions with dimensions (n_i, n_{eval}) .



(b) Schematic of Our Approach: We begin by learning the ground truth latent representations through reduced-order modeling. Next, we learn the operator in the latent space in a physics-informed manner using our Physics-Informed Latent Neural Operator (PI-Latent-NO) architecture. The framework consists of two coupled DeepONets: (1) A Latent DeepONet that maps n_i input functions to n_z -dimensional latent fields across $n_t + 1$ time steps, and (2) a Reconstruction DeepONet that transforms these latent fields into solution responses at n_x spatial locations, yielding outputs of shape $(n_i, n_t + 1, n_x)$. Key advantages: (i) Enables physics-informed training through automatic differentiation of temporal and spatial derivatives, and (ii) achieves linear scaling for large problems through inherent time-space separability, improving upon the quadratic scaling of PI-Vanilla-NO.

Figure 1: Comparison of Physics-Informed Neural Operator architectures: (a) The baseline PI-Vanilla-NO architecture and (b) our proposed PI-Latent-NO framework featuring coupled DeepONets for latent representation and solution reconstruction.

present the proposed physics-informed latent neural operator architecture and provide its theoretical foundations. Section 4 demonstrates the effectiveness of our approach through three benchmark problems, comparing its performance against traditional physics-informed DeepONet models in terms of prediction accuracy and computational efficiency. Finally, Section 5 summarizes our key findings and discusses future research directions.

2. Related Works

2.1. Neural Operators

In recent years, several neural operator regression methods have been proposed to learn mappings between functional spaces using neural networks. In 2019, Sharmila et al. [13] introduced a method for learning input-to-output function mappings using residual neural networks. However, theoretical guarantees for the universal approximation of operators had not yet been established at that time. Later, in 2021, Lu et al. [4] introduced DeepONet, which is based on the universal approximation theorem for operators by Chen and Chen [3], enabling the mapping between infinite-dimensional functions using neural nets. In the following years, additional operator regression methods based on integral transforms [8, 9, 10] were proposed. These advances will be discussed in detail below.

The DeepONet architecture features two neural networks: a branch net, which encodes the input functions at fixed sensor points, and a trunk net, which encodes the spatio-temporal coordinates of the output function. The solution operator is expressed as the inner product of the branch and trunk network outputs. The branch and trunk network outputs represent the coefficients and basis functions of the target output function, respectively. While DeepONets offer significant flexibility and the ability to learn solution operators for parametric PDEs, they also face challenges related to training complexity, data requirements, and long-time integration. Several modified DeepONet frameworks have been proposed to address these limitations [28, 29, 30, 5, 31, 32, 33, 34, 35, 36, 37].

Fourier Neural Operators (FNOs) [8, 38] employ neural networks combined with Fourier transforms to map input functions to target functions in the frequency domain. The core innovation of FNOs lies in their Fourier layer, which transforms the input into the frequency domain via the Fast Fourier Transform (FFT), applies a linear transformation to the lower Fourier modes, and filters out the higher modes. The inverse FFT then reconstructs the filtered representation back into the spatial domain. Despite their efficiency and flexibility for various parametric PDE problems, FNOs encounter challenges with non-periodic, heterogeneous, or high-frequency problems, as well as computational scalability, data requirements, and interpretability.

Wavelet Neural Operators (WNOs) [9, 39] integrate wavelet transforms with neural networks, decomposing functions into multi-scale representations that capture local and global features more effectively. Their architecture involves applying a wavelet transform to input data, extracting multi-scale features, and processing them through layers before applying an inverse wavelet transform to map the output back to the solution space. While WNOs enhance computational efficiency and flexibility, challenges remain in training and selecting suitable wavelet bases.

These operator learning methods have demonstrated promising results across various applications [40, 41, 42, 43, 44, 45, 39, 46]. However, their effectiveness in solving complex parametric PDEs is constrained by three key challenges: (1) performance deterioration with increasing system size and complexity, (2) the requirement for substantial paired input-output data, making large-scale dataset generation expensive and time-consuming, and (3) approximate solution operators that do not necessarily satisfy the governing PDEs.

To address the challenge of scaling to complex systems, recent advancements in latent space operator methods have shown promise. These methods accelerate computations by

learning operators in low-dimensional latent spaces. The approach typically involves dimensionality reduction to obtain a latent representation, followed by operator learning within this reduced space. Several studies have explored operator learning in latent spaces using DeepONets [1, 25, 2]. Wang et al. [47, 48] employed cross-attention-based encoders to project inputs into latent space, followed by transformer layers for operator learning, and decoded the outputs back into the original space using inverse cross-attention. Meng et al. [49] proposed a reduced-order neural operator on Riemannian manifolds.

Despite their potential, these architectures rely heavily on data-driven training, necessitating large datasets. Physics-informed training, which incorporates PDEs into the loss function, offers a pathway to addressing the second and third challenges. Several works have explored physics-informed variants of operator learning methods [50, 11, 27, 51, 52, 53]. However, scaling physics-informed training to large and complex problems remains computationally challenging, and existing latent neural operator architectures often lack compatibility with such physics-informed training approaches.

2.2. Reduced-Order Models (ROMs)

Reduced-order models (ROMs) [54] are indispensable tools for accelerating high-fidelity simulations of complex physical systems by projecting these systems onto lower-dimensional subspaces, thereby reducing computational costs while maintaining sufficient accuracy for real-time applications, uncertainty quantification, and optimization. One of the earliest techniques in dimensionality reduction is Principal Component Analysis (PCA) [55], which identifies the principal directions of variance in the data by finding orthogonal eigenvectors of the covariance matrix. PCA is widely used for its simplicity and effectiveness in handling linear systems, providing a foundation for many ROM techniques. A more advanced approach derived from PCA is Proper Orthogonal Decomposition (POD), which identifies orthogonal basis functions by decomposing datasets into principal components. Early work by Willcox et al. [56, 57] demonstrated its effectiveness in fields such as aerodynamics [58], fluid dynamics [59], and control systems [60]. More recently, autoencoders have emerged as powerful alternatives, leveraging neural networks to learn efficient, low-dimensional representations of complex systems. Unlike POD, autoencoders can capture non-linear relationships within the data, enabling accurate approximations for highly non-linear systems. Consisting of an encoder to project input data into a compressed latent space and a decoder to reconstruct the original data, autoencoder-based ROMs have been successfully applied in fluid dynamics to model turbulent flows [61], in structural damage detection [62], and in climate data fusion [63] offering greater flexibility in handling non-linearity and variability for modern simulation, optimization, and control tasks.

3. Methodology

This work focuses on accelerating simulations of physical systems described by high-dimensional PDEs. We consider PDEs of the following general form, which encompasses

time-dependent dynamics, initial conditions, and boundary constraints, expressed as:

$$\begin{cases} \frac{\partial u}{\partial t} + \mathcal{N}\left(u, \frac{\partial u}{\partial t}, \frac{\partial u}{\partial \mathbf{x}}, \frac{\partial^2 u}{\partial \mathbf{x}^2}, \dots, t, \mathbf{x}, \gamma(t, \mathbf{x})\right) = 0, & \text{in } \Omega \times (0, T], \\ u(0, \mathbf{x}) = g(\mathbf{x}), & \text{for } \mathbf{x} \in \Omega, \\ \mathcal{B}\left(u, \frac{\partial u}{\partial \mathbf{x}}, t, \mathbf{x}, \gamma\right) = 0, & \text{on } \partial\Omega \times (0, T], \end{cases} \quad (1)$$

where \mathcal{N} is the nonlinear PDE operator, u is the solution field varying in space and time, and γ is the input field varying in space and time, which could represent fields such as conductivity, source, or velocity depending on the PDE considered. Here, Ω denotes the spatial domain, T is the time duration, $g(\mathbf{x})$ specifies the initial condition, and \mathcal{B} is the boundary condition operator defined on $\partial\Omega$. Our research primarily addresses scenarios where the input field γ or the initial condition $g(\mathbf{x})$ is a random stochastic field. We represent the discretized version of these random stochastic fields by ξ . The main objective of this work is to efficiently learn the mapping between these stochastic input configurations ξ and the corresponding resultant solution fields u using our PI-Latent-NO model.

The procedure for learning these mappings is as follows. First, we sample n_{train} random input configurations ξ (note that n_{train} is a relatively small number compared to purely data-driven training) and obtain the corresponding ground truth trajectories of the PDEs. These ground truth solution trajectories are assumed to be sampled at fixed discrete time intervals Δt . Each ground-truth trajectory is then given by the time-ordered set:

$$\mathcal{T}_{u,i} = \left[\mathbf{u}_0^{(i)}, \mathbf{u}_{1\Delta t}^{(i)}, \mathbf{u}_{2\Delta t}^{(i)}, \dots, \mathbf{u}_{n_t\Delta t}^{(i)} \right], \quad i = 1, \dots, n_{\text{train}}, \quad (2)$$

where n_t denotes the length of the training trajectory. Here, $\mathbf{u}_a \in \mathbb{R}^{n_{\mathbf{x}}}$ represents the solution field of the PDE at time $t = a$, and $n_{\mathbf{x}}$ refers to the dimensionality of the solution field at a given time, which is determined by the number of grid points in the spatial domain. Using these solution trajectories $\{\mathcal{T}_{u,i}\}_{i=1}^{n_{\text{train}}}$, we extract the latent field representation of the solution field at time $t = a$ as $\mathbf{z}_a \in \mathbb{R}^{n_z}$, using dimensionality reduction techniques such as Principal Component Analysis (PCA), Proper Orthogonal Decomposition (POD), autoencoders, etc., where n_z represents the dimensionality of the latent field at a given time. For instance, by employing an autoencoder, we learn the latent representation \mathbf{z}_a (the encoder's output) by minimizing the reconstruction loss function:

$$\mathcal{L}(\boldsymbol{\theta}_{\text{AE}}) = \frac{1}{n_{\text{train}}(n_t + 1)n_{\mathbf{x}}} \sum_{i=1}^{n_{\text{train}}} \sum_{j=0}^{n_t} \left\| \mathbf{u}_{j\Delta t}^{(i)} - \tilde{\mathbf{u}}_{j\Delta t}^{(i)} \right\|_2^2, \quad (3)$$

where $\tilde{\mathbf{u}}$ denotes the decoder's output. This process yields the latent trajectories:

$$\mathcal{T}_{z,i} = \left[\mathbf{z}_0^{(i)}, \mathbf{z}_{1\Delta t}^{(i)}, \mathbf{z}_{2\Delta t}^{(i)}, \dots, \mathbf{z}_{n_t\Delta t}^{(i)} \right], \quad i = 1, \dots, n_{\text{train}}. \quad (4)$$

Following this, we learn the required mapping using our PI-Latent-NO architecture, shown in Figure 1b. This architecture comprises two stacked DeepONets: the Latent-DeepONet and the Reconstruction-DeepONet. The Latent-DeepONet learns the latent representations, while the Reconstruction-DeepONet reconstructs the solution in the original space. The key merits of this architecture are its ability to efficiently estimate low-dimensional latent spaces, which are crucial for managing the complexity of high-dimensional

systems. Additionally, as we see, with our architecture we can obtain derivatives such as $\left(\frac{\partial \hat{u}}{\partial t}, \frac{\partial \hat{u}}{\partial \mathbf{x}}, \frac{\partial^2 \hat{u}}{\partial \mathbf{x}^2}, \dots\right)$ via automatic differentiation (AD), enabling us to train the model in a physics-informed manner. These advantages enable the prediction of complex responses for various PDEs by learning operators in low-dimensional latent spaces in a physics-informed manner with relatively small sizes of data. We learn the network parameters, $\boldsymbol{\theta}$, of this architecture by minimizing the following loss function with data-driven and physics-informed loss components defined as:

$$\mathcal{L}(\boldsymbol{\theta}) = \mathcal{L}_{\text{data-driven}}(\boldsymbol{\theta}) + \mathcal{L}_{\text{physics-informed}}(\boldsymbol{\theta}), \quad (5)$$

where,

$$\begin{aligned} \mathcal{L}_{\text{data-driven}}(\boldsymbol{\theta}) &= \frac{1}{n_{\text{train}}(n_t + 1)n_{\mathbf{z}}} \sum_{i=1}^{n_{\text{train}}} \sum_{j=0}^{n_t} \left\| \mathbf{z}(\boldsymbol{\xi}^{(i)}, j\Delta t) - \hat{\mathbf{z}}(\boldsymbol{\xi}^{(i)}, j\Delta t) \right\|_2^2 \\ &+ \frac{1}{n_{\text{train}}(n_t + 1)n_{\mathbf{x}}} \sum_{i=1}^{n_{\text{train}}} \sum_{j=0}^{n_t} \sum_{k=1}^{n_{\mathbf{x}}} \left(u(\boldsymbol{\xi}^{(i)}, j\Delta t, \mathbf{x}^{(k)}) - \hat{u}(\boldsymbol{\xi}^{(i)}, j\Delta t, \mathbf{x}^{(k)}) \right)^2, \end{aligned} \quad (6)$$

$$\begin{aligned} \mathcal{L}_{\text{physics-informed}}(\boldsymbol{\theta}) &= \mathcal{L}_r(\boldsymbol{\theta}) + \mathcal{L}_{bc}(\boldsymbol{\theta}) + \mathcal{L}_{ic}(\boldsymbol{\theta}) \\ &= \frac{1}{n_i n_t^r n_{\mathbf{x}}^r} \sum_{i=1}^{n_i} \sum_{j=1}^{n_t^r} \sum_{k=1}^{n_{\mathbf{x}}^r} \left(\frac{\partial \hat{u}(\boldsymbol{\xi}^{(i)}, t^{(j)}, \mathbf{x}^{(k)})}{\partial t} + \mathcal{N}[\hat{u}](\boldsymbol{\xi}^{(i)}, t^{(j)}, \mathbf{x}^{(k)}) \right)^2 \\ &+ \frac{1}{n_i n_t^{bc} n_{\mathbf{x}}^{bc}} \sum_{i=1}^{n_i} \sum_{j=1}^{n_t^{bc}} \sum_{k=1}^{n_{\mathbf{x}}^{bc}} \left(\mathcal{B}[\hat{u}](\boldsymbol{\xi}^{(i)}, t^{(j)}, \mathbf{x}^{(k)}) \right)^2 \\ &+ \frac{1}{n_i n_{\mathbf{x}}^{ic}} \sum_{i=1}^{n_i} \sum_{k=1}^{n_{\mathbf{x}}^{ic}} \left(\hat{u}(\boldsymbol{\xi}^{(i)}, 0, \mathbf{x}^{(k)}) - g(\mathbf{x}^{(k)}) \right)^2. \end{aligned} \quad (7)$$

The data-driven loss function consists of two terms: the first term minimizes the mean squared error (MSE) between the ground truth latent field, $\mathbf{z}(\boldsymbol{\xi}^{(i)}, j\Delta t)$, obtained from the dimensionality reduction method in the first step, and the predicted latent response from our Latent-DeepONet, $\hat{\mathbf{z}}(\boldsymbol{\xi}^{(i)}, j\Delta t)$. The second term minimizes the MSE between the ground truth solution fields u , which were used to learn the latent fields in the previous step, and the predicted responses from our Reconstruction-DeepONet, \hat{u} .

The physics-informed loss term has three components: residual loss, boundary condition loss, and initial condition loss, all based on the PDE for n_i input functions sampled in each iteration. These loss terms are evaluated at the collocation points $\{t^{(j)}\}_{j=1}^{n_t^r} \{\mathbf{x}^{(k)}\}_{k=1}^{n_{\mathbf{x}}^r}$ within the domain, as well as at the collocation points $\{t^{(j)}\}_{j=1}^{n_t^{bc}} \{\mathbf{x}^{(k)}\}_{k=1}^{n_{\mathbf{x}}^{bc}}$ on the boundary and $\{\mathbf{x}^{(k)}\}_{k=1}^{n_{\mathbf{x}}^{ic}}$ at the initial condition.

Now, moving to how we estimate the gradients in the residual loss term, we can see from Figure 1b that the batch-based forward passes of our model reveal a mismatch in the leading dimensions of t , \mathbf{x} and \hat{u} . This dimension mismatch prevents the direct application of default reverse-mode AD in deep learning frameworks such as PyTorch and TensorFlow to compute

the necessary gradients $\left(\frac{\partial \hat{u}}{\partial t}, \frac{\partial \hat{u}}{\partial \mathbf{x}}, \frac{\partial^2 \hat{u}}{\partial \mathbf{x}^2}, \dots\right)$ for the residual loss term. To address this, one approach would involve reshaping these quantities to align their leading dimensions, enabling the use of reverse-mode AD, or alternatively, writing a custom reverse AD module with for loops to obtain the required gradients. However, this would increase computational overhead. Therefore, we employ forward-mode AD to estimate the necessary gradients efficiently. For instance, forward-mode AD enables us to directly estimate the gradient $\frac{\partial \hat{u}}{\partial t}$, which aligns with the shape of \hat{u} , as forward AD computes gradients by traversing the computational graph from left to right, avoiding the issue of leading dimension mismatch.

Comparing our architecture to the Vanilla DeepONet model in Figure 1a, we can clearly see that there is an inherent separability in time and space in our architecture, which provides substantial advantages. In large-scale problems where solution has to be evaluated at numerous time stamps and spatial coordinates — such as for example at 100 time stamps ($n_t = 100$) with a spatial grid of 512 points ($n_{\mathbf{x}} = 512$) — this separability becomes crucial. In this case, vanilla DeepONet model trunk network would need to be evaluated $n_{\text{eval}} = 100 \times 512$ times. In contrast, in our model, the trunk network for the latent DeepONet requires only 100 evaluations, and the reconstruction DeepONet trunk network requires 512 evaluations, resulting in a total of 612 evaluations. Thus, because of this separability, our approach scales linearly, in contrast to the quadratic scaling of the vanilla approach, making our method highly advantageous for solving very large physical problems.

The complete training process of our PI-Latent-NO model is outlined in detail in Algorithm 1.

4. Results

In this section, we demonstrate the effectiveness of our proposed framework in predicting solutions for various benchmark parametric PDE examples from the literature. We compare the performance of our model against the Vanilla DeepONet model trained in a purely physics-informed manner. A summary of the examples considered in this study is provided in Table 1. Details of the network architectures and hyperparameters used for both the Vanilla DeepONet model and our model are presented in Table A1 and Table A2, respectively. The code and data for all examples will be made publicly available upon publication. The training for all the examples shown was carried out on a GPU-based system with nodes featuring 4 Nvidia A100 GPUs, each with 40GB of memory. However, memory and runtime comparison studies in Example 1 were conducted on nodes with 4 Nvidia A100 GPUs, each with 80GB of memory.

In this work, the performance of the models is evaluated on the test samples using the mean squared error (MSE), defined as:

$$\text{MSE}_{\text{test}} = \frac{1}{n_{\text{test}} n_t n_{\mathbf{x}}} \sum_{i=1}^{n_{\text{test}}} \sum_{j=1}^{n_t} \sum_{k=1}^{n_{\mathbf{x}}} \left(u(\boldsymbol{\xi}^{(i)}, t^{(j)}, \mathbf{x}^{(k)}) - \hat{u}(\boldsymbol{\xi}^{(i)}, t^{(j)}, \mathbf{x}^{(k)}) \right)^2, \quad (8)$$

where i indexes all test samples, j and k indexes over all the spatiotemporal locations at which the PDE solution is available. Here u and \hat{u} are the ground-truth and the predicted values of the solution field, respectively.

Algorithm 1 Training Algorithm for PI-Latent-NO

- 1: **Input:** A set of input functions $\{\xi_i\}_{i=1}^n$; subset size n_{train} ; training data $\mathcal{D}_{\text{train}} = \{(\xi_i, \mathcal{T}_{u,i})\}_{i=1}^{n_{\text{train}}}$, where ξ_i is the i -th input function, and $\mathcal{T}_{u,i} = [\mathbf{u}_0^{(i)}, \mathbf{u}_{\Delta t}^{(i)}, \mathbf{u}_{2\Delta t}^{(i)}, \dots, \mathbf{u}_{n_t \Delta t}^{(i)}]$ is the corresponding output trajectory at different time steps; neural network architectures for the branch and trunk networks of the Latent and Reconstruction DeepONets; number of epochs n_{epochs} ; batch size bs ; number of batches $n_{\text{batch}} = \lceil n / bs \rceil$; and learning rate α .
- 2: **Step 1:** Learn the latent trajectory of the output function at each time step for all training data, i.e., $\{\mathcal{T}_{z,i}\}_{i=1}^{n_{\text{train}}}$, where $\mathcal{T}_{z,i} = [\mathbf{z}_0^{(i)}, \mathbf{z}_{\Delta t}^{(i)}, \mathbf{z}_{2\Delta t}^{(i)}, \dots, \mathbf{z}_{n_t \Delta t}^{(i)}]$, using reduced-order modeling techniques:
- 3: a) **Using PCA:**

$$\mathcal{L}(\mathbf{W}) = \frac{1}{n_{\text{train}}(n_t + 1)n_{\mathbf{x}}} \sum_{i=1}^{n_{\text{train}}} \sum_{j=0}^{n_t} \left\| \mathbf{u}_{j \Delta t}^{(i)} - \tilde{\mathbf{u}}_{j \Delta t}^{(i)} \right\|_2^2,$$

where $\tilde{\mathbf{u}}_{j \Delta t}^{(i)} = \mathbf{W} \mathbf{W}^T \mathbf{u}_{j \Delta t}^{(i)}$ is the reconstruction of $\mathbf{u}_{j \Delta t}^{(i)}$ using the principal components, and \mathbf{W} is the matrix of principal components obtained from the SVD. The latent representation of the solution at time step $j \Delta t$ is given by:

$$\mathbf{z}_{j \Delta t}^{(i)} = \mathbf{W}_{d_{\mathbf{z}}}^T \mathbf{u}_{j \Delta t}^{(i)},$$

where $\mathbf{W}_{d_{\mathbf{z}}}$ is the matrix of $d_{\mathbf{z}}$ principal components.

- 4: b) **Using Autoencoder:** Train the Autoencoder by minimizing the loss:

$$\mathcal{L}(\boldsymbol{\theta}_{\text{AE}}) = \frac{1}{n_{\text{train}}(n_t + 1)n_{\mathbf{x}}} \sum_{i=1}^{n_{\text{train}}} \sum_{j=0}^{n_t} \left\| \mathbf{u}_{j \Delta t}^{(i)} - \tilde{\mathbf{u}}_{j \Delta t}^{(i)} \right\|_2^2,$$

where $\tilde{\mathbf{u}}_{j \Delta t}^{(i)} = \text{Decoder}(\mathbf{z}_{j \Delta t}^{(i)})$ and $\mathbf{z}_{j \Delta t}^{(i)} = \text{Encoder}(\mathbf{u}_{j \Delta t}^{(i)})$.

- 5: **Step 2:** Train the PI-Latent-NO model.

- 6: **for** epoch = 1 to n_{epochs} **do**
- 7: Shuffle n input functions.
- 8: **for** batch = 1 to n_{batch} **do**
- 9: start \leftarrow (batch - 1) \times bs + 1, end \leftarrow min(batch \times bs, n).
- 10: Randomly sample $(n_t^r, n_{\mathbf{x}}^r)$ spatiotemporal collocation points from the domain, $(n_t^{bc}, n_{\mathbf{x}}^{bc})$ points from the boundary, and $(n_{\mathbf{x}}^{ic})$ points at the initial time.
- 11: Compute the total loss:

$$\mathcal{L}(\boldsymbol{\theta}) = \mathcal{L}_{\text{data-driven}}(\boldsymbol{\theta}) + \mathcal{L}_{\text{physics-informed}}(\boldsymbol{\theta}),$$

where

$$\begin{aligned} \mathcal{L}_{\text{data-driven}}(\boldsymbol{\theta}) &= \frac{1}{n_{\text{train}}(n_t + 1)n_{\mathbf{z}}} \sum_{i=1}^{n_{\text{train}}} \sum_{j=0}^{n_t} \left\| \mathbf{z}(\xi^{(i)}, j \Delta t) - \hat{\mathbf{z}}(\xi^{(i)}, j \Delta t) \right\|_2^2 \\ &+ \frac{1}{n_{\text{train}}(n_t + 1)n_{\mathbf{x}}} \sum_{i=1}^{n_{\text{train}}} \sum_{j=0}^{n_t} \sum_{k=1}^{n_{\mathbf{x}}} \left(\hat{u}(\xi^{(i)}, j \Delta t, \mathbf{x}^{(k)}) - \hat{u}(\xi^{(i)}, j \Delta t, \mathbf{x}^{(k)}) \right)^2, \end{aligned}$$

$$\begin{aligned} \mathcal{L}_{\text{physics-informed}}(\boldsymbol{\theta}) &= \mathcal{L}_r(\boldsymbol{\theta}) + \mathcal{L}_{bc}(\boldsymbol{\theta}) + \mathcal{L}_{ic}(\boldsymbol{\theta}) \\ &= \frac{1}{(end - start + 1)n_t^r n_{\mathbf{x}}^r} \sum_{i=start}^{end} \sum_{j=1}^{n_t^r} \sum_{k=1}^{n_{\mathbf{x}}^r} \left(\frac{\partial \hat{u}(\xi^{(i)}, t^{(j)}, \mathbf{x}^{(k)})}{\partial t} + \mathcal{N}[\hat{u}](\xi^{(i)}, t^{(j)}, \mathbf{x}^{(k)}) \right)^2 \\ &+ \frac{1}{(end - start + 1)n_t^{bc} n_{\mathbf{x}}^{bc}} \sum_{i=start}^{end} \sum_{j=1}^{n_t^{bc}} \sum_{k=1}^{n_{\mathbf{x}}^{bc}} \left(\mathcal{B}[\hat{u}](\xi^{(i)}, t^{(j)}, \mathbf{x}^{(k)}) \right)^2 \\ &+ \frac{1}{(end - start + 1)n_{\mathbf{x}}^{ic}} \sum_{i=start}^{end} \sum_{k=1}^{n_{\mathbf{x}}^{ic}} \left(\hat{u}(\xi^{(i)}, 0, \mathbf{x}^{(k)}) - g(\mathbf{x}^{(k)}) \right)^2, \end{aligned}$$

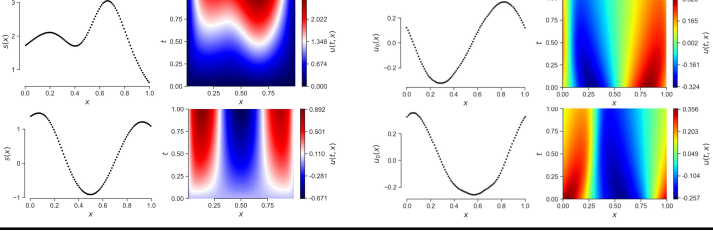
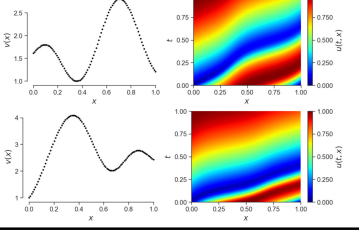
and $\hat{\mathbf{z}}$, \hat{u} are the outputs of the Latent DeepONet and Reconstruction DeepONet, respectively.

- 12: Backpropagate the loss through the networks and update the weights of the PI-Latent-NO model:

$$\boldsymbol{\theta} \leftarrow \boldsymbol{\theta} - \alpha \nabla_{\boldsymbol{\theta}} \mathcal{L}(\boldsymbol{\theta}).$$

- 13: **end for**
- 14: **end for**
- 15: **Output:** Trained PI-Latent-NO model.

Table 1: Schematic of operator learning benchmarks under consideration in this work.

Case	Diffusion-reaction dynamics	Burgers' transport dynamics	Advection
PDE	$\frac{\partial u}{\partial t} = D \frac{\partial^2 u}{\partial x^2} + k u^2 + s(x),$ $D = 0.01, \quad k = 0.01,$ $(t, x) \in (0, 1] \times (0, 1],$ $u(0, x) = 0, \quad x \in (0, 1)$ $u(t, 0) = 0, \quad t \in (0, 1)$ $u(t, 1) = 0, \quad t \in (0, 1)$ $\mathcal{G}_\theta : s(x) \rightarrow u(t, x).$	$\frac{\partial u}{\partial t} + u \frac{\partial u}{\partial x} - \nu \frac{\partial^2 u}{\partial x^2} = 0,$ $\nu = 0.01,$ $(t, x) \in (0, 1] \times (0, 1],$ $u(0, x) = g(x), \quad x \in (0, 1)$ $u(t, 0) = u(t, 1)$ $\frac{\partial u}{\partial x}(t, 0) = \frac{\partial u}{\partial x}(t, 1)$ $\mathcal{G}_\theta : g(x) \rightarrow u(t, x).$	$\frac{\partial u}{\partial t} + s(x) \frac{\partial u}{\partial x} = 0,$ $(t, x) \in (0, 1] \times (0, 1],$ $u(0, x) = \sin(\pi x) \quad \forall x \in (0, 1),$ $u(t, 0) = \sin(0.5\pi t) \quad \forall t \in (0, 1),$ $s(x) = v(x) - \min_x v(x) + 1$ $\mathcal{G}_\theta : v(x) \rightarrow u(t, x).$
Input Function	$s(x) \sim \text{GP}(0, k(x, x')),$ $\ell_x = 0.2, \quad \sigma^2 = 1.0,$ $k(x, x') = \sigma^2 \exp \left\{ -\frac{\ x - x'\ ^2}{2\ell_x^2} \right\}.$	$g(x) \sim \mathcal{N} \left(0, 25^2 (-\Delta + 5^2 I)^{-4} \right),$	$v(x) \sim \text{GP}(0, k(x, x')),$ $\ell_x = 0.2, \quad \sigma^2 = 1.0,$ $k(x, x') = \sigma^2 \exp \left\{ -\frac{\ x - x'\ ^2}{2\ell_x^2} \right\}.$
Samples			

4.1. Example - 1D Diffusion-Reaction Dynamics

In this example, we consider a diffusion-reaction system governed by the following equation:

$$\begin{aligned}
\frac{\partial u}{\partial t} &= D \frac{\partial^2 u}{\partial x^2} + k u^2 + s(x), \quad (t, x) \in (0, 1] \times (0, 1], \\
u(0, x) &= 0 \quad \forall x \in (0, 1), \\
u(t, 0) &= 0 \quad \forall t \in (0, 1), \\
u(t, 1) &= 0 \quad \forall t \in (0, 1),
\end{aligned} \tag{9}$$

where $D = 0.01$ is the diffusion coefficient and $k = 0.01$ is the reaction coefficient. The source term $s(x)$ is modeled as a random field generated from a Gaussian random process. The goal is to learn the solution operator that maps these random source terms $s(x)$ to their corresponding solutions $u(t, x)$, i.e., $\mathcal{G}_\theta : s(x) \rightarrow u(t, x)$.

A total of 2,500 input source field functions were generated. Of these, 2,000 were used for training, with ground-truth solutions estimated for $n_{\text{train}} \in \{50, 100, 150, 200\}$ input functions. The remaining $n_{\text{test}} = 500$ input functions were used for testing, with their ground-truth solutions also estimated. Each source function was discretized at 100 equally spaced spatial points, while the solution field was discretized at $n_t + 1 = 101$ time points and $n_x = 100$ spatial points, resulting in a grid of 101×100 points.

Using the n_{train} ground-truth solution fields, the corresponding latent fields ($n_z = 9$) were extracted using both PCA and autoencoder-based dimensionality reduction methods, which were then employed in the data-driven loss term of our model. Both the Vanilla DeepONet model and our proposed model were trained for 8,000 epochs, and this process was repeated across five independent trials, each using a different random seed.

Figure 2 compares all models for a representative test sample. Table 2 presents the performance metrics, while Figure 3 illustrates the box plots of the MSE for the test data alongside the corresponding training times. It is noteworthy that, for the Vanilla DeepONet model, $n_{\text{train}} = 0$ as it is trained in a purely physics-informed manner. The test MSE for all models is consistent around 10^{-4} , while the training time is higher for our proposed model due to the additional computational burden of training two stacked DeepONets.

Nevertheless, subsequent studies demonstrate that, as the number of spatiotemporal locations used for physics-informed loss evaluation increases, the training time and memory usage for the Vanilla DeepONet model increase significantly. In contrast, the training time and memory consumed by our model remain nearly constant. This consistency in computational efficiency arises from the separability of time and space in our model’s architecture, as previously discussed.

We carried out an ablation study by varying the number of collocation points within the solution space ($n_t^r \times n_x^r$) from 8^2 to 1024^2 , keeping $n_{\text{train}} = 200$ and $n_t^r = n_x^r = n_t^{bc} = n_x^i$ with $n_x^{bc} = 1$ for each boundary. As shown in Figure 4, the runtime per iteration and memory consumption are nearly independent of the solution space discretization with our PI-Latent-NO model.

Similarly, another ablation study is carried out by keeping the number of collocation points along the temporal axis fixed at $n_t^r = 64$ and by varying the number of collocation points along the spatial direction n_x^r from 8 to 4096. We kept $n_{\text{train}} = 200$ with $n_t^{bc} = 64$, $n_x^{bc} = 1$ for each boundary and $n_x^i = n_x^r$. Figure 5 shows that the runtime per iteration and memory consumption remains constant with our method, providing a significant advantage when solving large physical problems with increasing mesh size and finer discretizations.

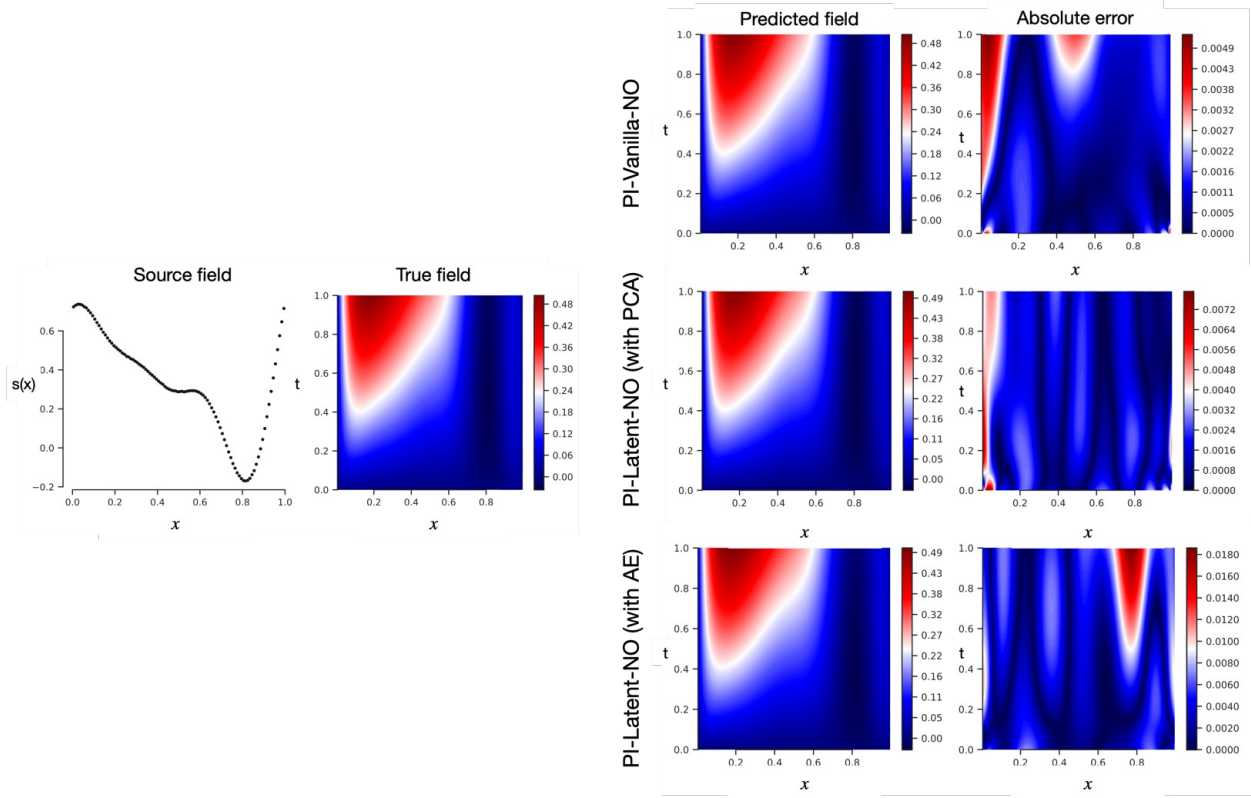
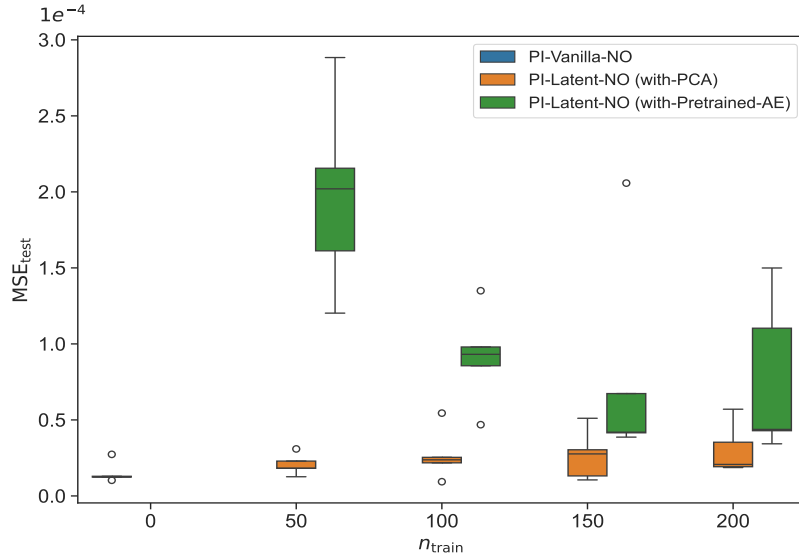
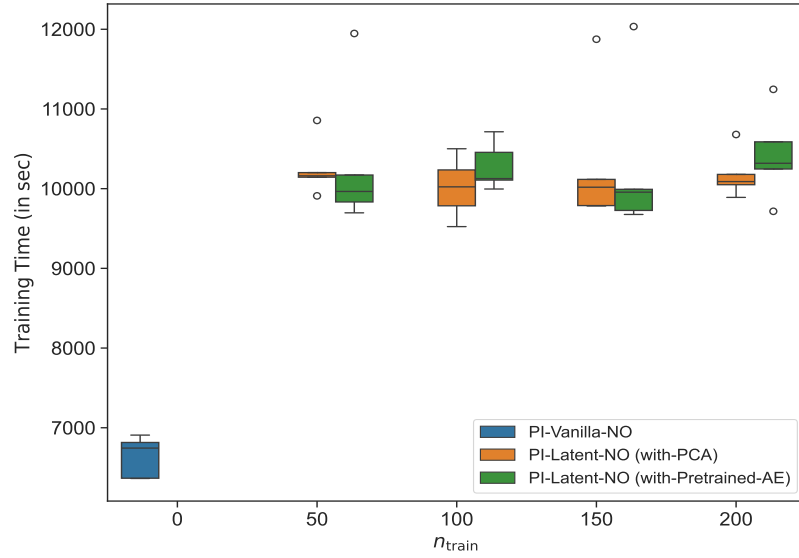


Figure 2: 1D Diffusion-reaction dynamics: Comparison of all models for a representative test sample, using $n_{\text{train}} = 200$ training samples for our model training.



(a)

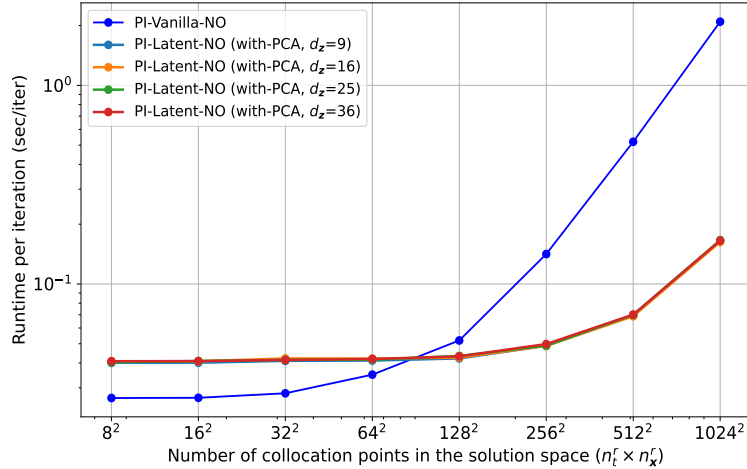


(b)

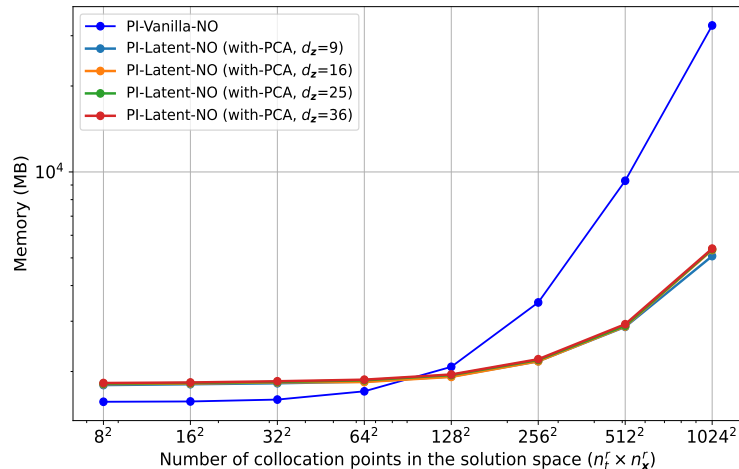
Figure 3: For the 1D Diffusion-reaction dynamics: (a) presents the mean squared error of the test data, and (b) shows the training time. The results are based on 5 independent runs with different seeds, varying the number of training samples n_{train} .

Table 2: 1D Diffusion-reaction dynamics: Performance metrics

Model	n_{train}	MSE_{test}
PI-Vanilla-NO	0	$1.5\text{e-}05 \pm 6.9\text{e-}06$
PI-Latent-NO (with-PCA)	50	$2.1\text{e-}05 \pm 6.8\text{e-}06$
PI-Latent-NO (with-Pretrained-AE)	50	$2.0\text{e-}04 \pm 6.3\text{e-}05$
PI-Latent-NO (with-PCA)	100	$2.7\text{e-}05 \pm 1.7\text{e-}05$
PI-Latent-NO (with-Pretrained-AE)	100	$9.2\text{e-}05 \pm 3.1\text{e-}05$
PI-Latent-NO (with-PCA)	150	$2.7\text{e-}05 \pm 1.6\text{e-}05$
PI-Latent-NO (with-Pretrained-AE)	150	$7.9\text{e-}05 \pm 7.2\text{e-}05$
PI-Latent-NO (with-PCA)	200	$3.0\text{e-}05 \pm 1.7\text{e-}05$
PI-Latent-NO (with-Pretrained-AE)	200	$7.6\text{e-}05 \pm 5.1\text{e-}05$

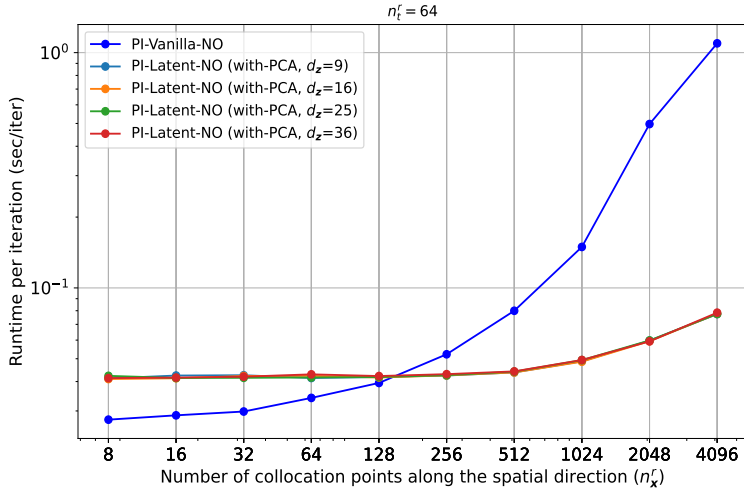


(a)

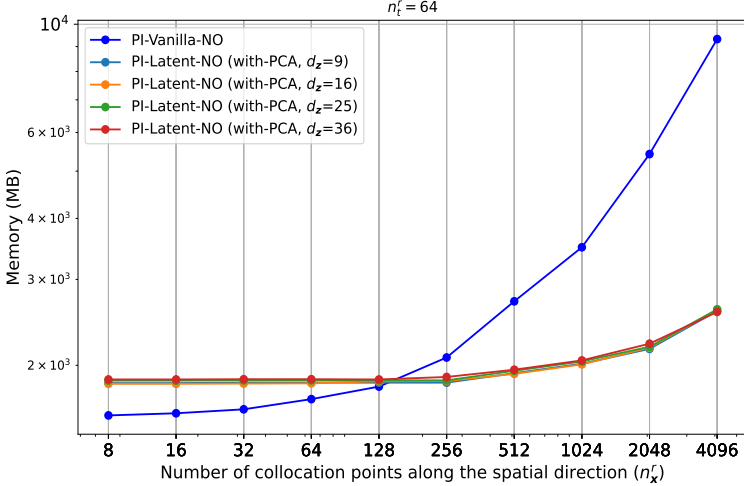


(b)

Figure 4: For the 1D Diffusion-reaction dynamics: (a) presents the runtime per iteration (seconds/iteration), and (b) shows the memory (MB). The results are based on varying the number of collocation points in the solution space.



(a)



(b)

Figure 5: For the 1D Diffusion-reaction dynamics: (a) illustrates the runtime per iteration (seconds per iteration), and (b) depicts the memory usage (MB). The results are obtained by varying the number of collocation points along the spatial direction while keeping the number of collocation points along the temporal axis fixed at $n_t^r = 64$.

4.2. 1D Burgers' Transport Dynamics

To highlight the proposed framework's capability to handle non-linearity in governing PDEs, we consider the one-dimensional (1D) Burgers' equation with periodic boundary

conditions:

$$\begin{aligned}
\frac{\partial u}{\partial t} + u \frac{\partial u}{\partial x} - \nu \frac{\partial^2 u}{\partial x^2} &= 0, \quad (t, x) \in (0, 1) \times (0, 1] \\
u(0, x) &= g(x), \quad x \in (0, 1) \\
u(t, 0) &= u(t, 1) \\
\frac{\partial u}{\partial x}(t, 0) &= \frac{\partial u}{\partial x}(t, 1)
\end{aligned} \tag{10}$$

where $t \in (0, 1)$, the viscosity ν is set to $\nu = 0.01$, and the initial condition $g(x)$ is generated from a Gaussian Random Field (GRF) satisfying the periodic boundary conditions. The objective is to learn the mapping between the initial condition $g(x)$ and the solution field $u(t, x)$, i.e., $\mathcal{G}_\theta : g(x) \rightarrow u(t, x)$.

In a manner similar to the previous example, a total of 2,500 initial condition functions were generated for this case. Out of these, 2,000 functions were designated for training, with ground-truth solutions estimated for $n_{\text{train}} = 200$ selected inputs. The remaining $n_{\text{test}} = 500$ functions were reserved for testing purposes, with ground-truth solutions calculated for them as well. The initial condition functions are discretized at 101 equally spaced spatial points and the solution field was resolved across $n_t + 1 = 101$ time steps and $n_x = 101$ spatial locations, resulting in a 101×101 grid.

From the n_{train} ground-truth solutions and the 2,000 training initial conditions, corresponding latent fields (with a dimensionality of $n_z = 9$) were obtained using both PCA and autoencoder techniques. With access to the latent representation of the initial conditions, we shift our approach: rather than learning a mapping between the initial condition and the solution field, we instead learn a mapping from the latent initial condition to the solution field.

Both the Vanilla DeepONet model and our proposed model were trained using five different random seeds. Table 3 shows the performance metrics, where similar behavior in test MSE is observed, consistent with the previous example. Figure 6 provides a comparison of model predictions for a representative test sample.

Table 3: 1D Burgers transport dynamics: Performance metrics

Model	n_{train}	MSE_{test}
PI-Vanilla-NO	0	$6.1\text{e-}04 \pm 8.4\text{e-}05$
PI-Latent-NO (with-PCA)	200	$5.5\text{e-}04 \pm 1.3\text{e-}04$
PI-Latent-NO (with-Pretrained-AE)	200	$6.7\text{e-}04 \pm 1.3\text{e-}04$

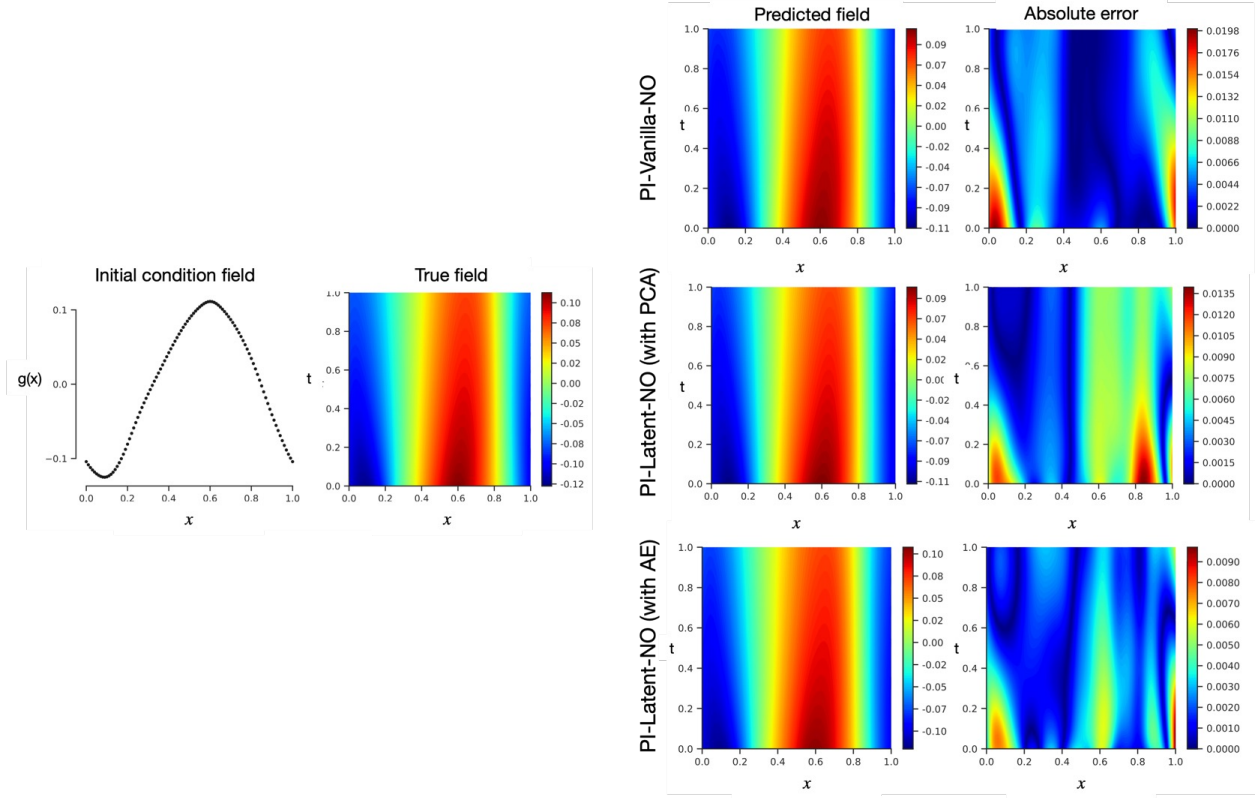


Figure 6: 1D Burgers' transport dynamics: Model comparison for a representative test sample with $n_{\text{train}} = 200$ training samples used in our model.

4.3. 1D Advection

Next, we consider a linear advection equation with variable coefficients:

$$\begin{aligned}
 \frac{\partial u}{\partial t} + s(x) \frac{\partial u}{\partial x} &= 0, \quad (t, x) \in (0, 1] \times (0, 1], \\
 u(0, x) &= g(x) \quad \forall x \in (0, 1), \\
 u(t, 0) &= f(t) \quad \forall t \in (0, 1),
 \end{aligned} \tag{11}$$

where $g(x) = \sin(\pi x)$ and $f(t) = \sin(0.5\pi t)$. To ensure positivity of $s(x)$, we set $s(x) = v(x) - \min_x v(x) + 1$, with $v(x)$ sampled from a GRF. The objective here is to learn the mapping between the advection speed $s(x)$ and the solution field $u(t, x)$, i.e., $\mathcal{G}_{\theta} : s(x) \rightarrow u(t, x)$.

Using the same setup as previous examples, a total of 2,500 advection speed functions were generated. Of these, 2,000 functions were designated for training, with ground-truth solutions computed for $n_{\text{train}} = 200$ selected inputs. The remaining $n_{\text{test}} = 500$ functions were reserved for testing, with corresponding ground-truth solutions also estimated. The advection speed functions were discretized over 100 equally spaced spatial points, while the solution fields were discretized in time with $n_t + 1 = 100$ time steps and spatially with $n_x = 100$ spatial locations, resulting in a grid of size 100×100 . Latent fields of dimension $n_z = 9$ were extracted from the n_{train} ground-truth solutions using PCA and autoencoder techniques and incorporated into the model's data-driven loss term.

Both models were trained across five trials with different random seeds. Table 4 presents the performance metrics, showing consistent test MSE behavior with the previous example. Figure 7 illustrates a comparison of model predictions for a representative test sample.

Table 4: 1D Advection: Performance metrics

Model	n_{train}	MSE_{test}
PI-Vanilla-NO	0	$5.1\text{e-}04 \pm 2.1\text{e-}05$
PI-Latent-NO (with-PCA)	200	$4.7\text{e-}04 \pm 6.0\text{e-}05$
PI-Latent-NO (with-Pretrained-AE)	200	$5.7\text{e-}04 \pm 4.9\text{e-}05$

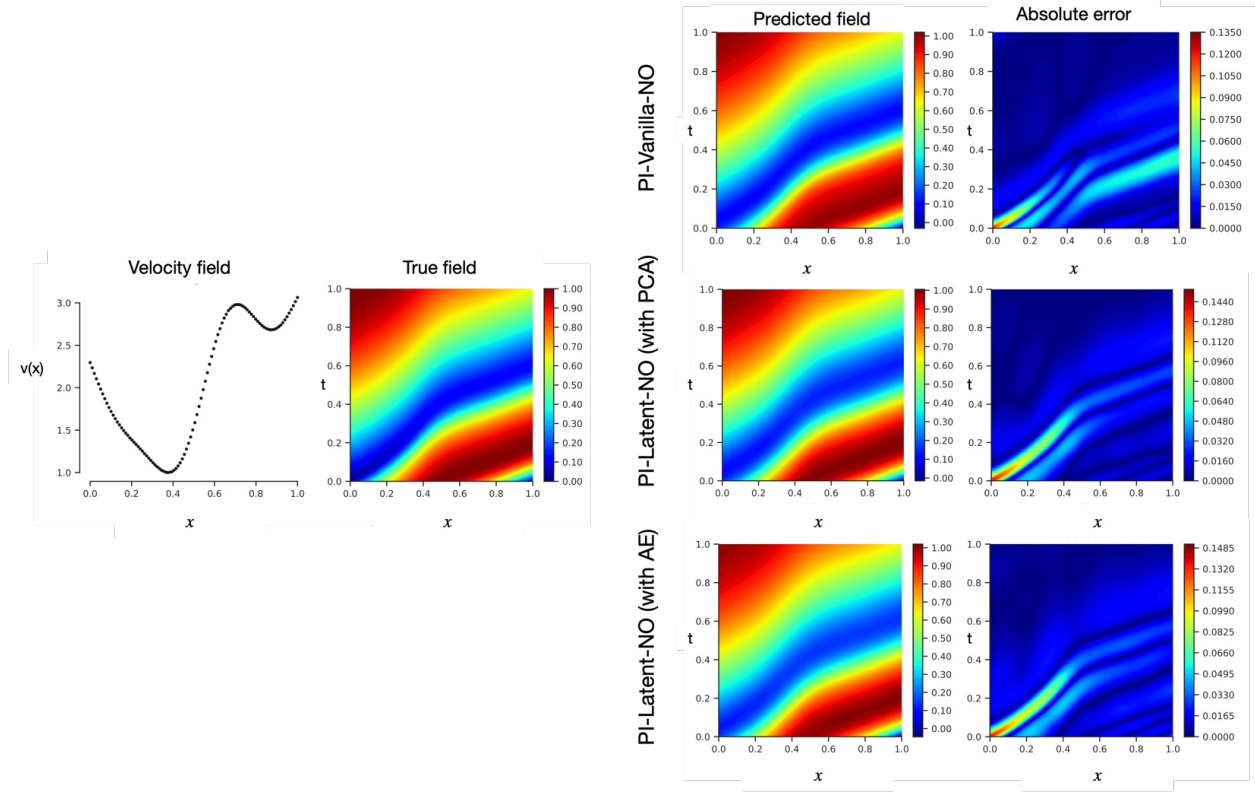


Figure 7: 1D Advection dynamics: Comparison of model predictions for a representative test sample with $n_{\text{train}} = 200$ training samples used for training our model.

5. Summary

In this work, we addressed the key limitations of existing Latent DeepONet [2, 1] architectures, which rely on large datasets for data-driven training and cannot incorporate governing physics due to the two-step training process. To overcome these challenges, we introduced PI-Latent-NO, a physics-informed latent operator learning framework. This end-to-end architecture employs two coupled DeepONets: the *Latent-DeepONet*, which identifies and learns a low-dimensional latent space, and the *Reconstruction-DeepONet*, which maps the latent representations back to the original physical space. This architecture offers two key advantages:

- It facilitates physics-informed training by enabling the computation of temporal and spatial derivatives through automatic differentiation, thereby reducing over-reliance on labeled dataset for training.
- It exploits the separability of spatial and temporal components, achieving approximately linear computational scaling even for large-scale systems, compared to the quadratic scaling of physics-informed Vanilla DeepONet models.

Our results demonstrate the effectiveness of PI-Latent-NO as a proof of concept in learning mappings for high-dimensional parametric PDEs. The framework consistently captures complex system dynamics with high accuracy, while optimizing computational and memory efficiency. Moreover, it effectively reduces redundant features by leveraging the latent space, enabling faster convergence. In conclusion, the PI-Latent-NO framework represents a transformative step in physics-informed machine learning. By seamlessly integrating latent space representation with governing physics, it sets a new standard for tackling high-dimensional PDEs, offering scalable and accurate solutions for future advancements in scientific computing.

Acknowledgements: We express our sincere gratitude to Professor Yannis Kevrekidis and Professor Michael Shields for their insightful discussions and invaluable guidance, which have significantly contributed to the development of this work. This work has been made possible by the financial support provided by the U.S. Department of Energy, Office of Science, Office of Advanced Scientific Computing Research, under Award Number DE-SC0024162.

References

- [1] V. Oommen, K. Shukla, S. Goswami, R. Dingreville, G. E. Karniadakis, Learning two-phase microstructure evolution using neural operators and autoencoder architectures, *npj Computational Materials* 8 (1) (2022) 190.
- [2] K. Kontolati, S. Goswami, G. Em Karniadakis, M. D. Shields, Learning nonlinear operators in latent spaces for real-time predictions of complex dynamics in physical systems, *Nature Communications* 15 (1) (2024) 5101.
- [3] T. Chen, H. Chen, Universal approximation to nonlinear operators by neural networks with arbitrary activation functions and its application to dynamical systems, *IEEE Transactions on Neural Networks* 6 (4) (1995) 911–917.
- [4] L. Lu, P. Jin, G. Pang, Z. Zhang, G. E. Karniadakis, Learning nonlinear operators via DeepONet based on the universal approximation theorem of operators, *Nature machine intelligence* 3 (3) (2021) 218–229.
- [5] B. Bahmani, S. Goswami, I. G. Kevrekidis, M. D. Shields, A Resolution Independent Neural Operator, *arXiv preprint arXiv:2407.13010* (2024).
- [6] T. Ingebrand, A. J. Thorpe, S. Goswami, K. Kumar, U. Topcu, Basis-to-basis operator learning using function encoders, *arXiv preprint arXiv:2410.00171* (2024).

- [7] A. Anandkumar, K. Azizzadenesheli, K. Bhattacharya, N. Kovachki, Z. Li, B. Liu, A. Stuart, Neural operator: Graph kernel network for partial differential equations, in: ICLR 2020 Workshop on Integration of Deep Neural Models and Differential Equations, 2020.
- [8] Z. Li, N. Kovachki, K. Azizzadenesheli, B. Liu, K. Bhattacharya, A. Stuart, A. Anandkumar, Fourier neural operator for parametric partial differential equations, arXiv preprint arXiv:2010.08895 (2020).
- [9] T. Tripura, S. Chakraborty, Wavelet neural operator: a neural operator for parametric partial differential equations, arXiv preprint arXiv:2205.02191 (2022).
- [10] Q. Cao, S. Goswami, G. E. Karniadakis, Laplace neural operator for solving differential equations, *Nature Machine Intelligence* 6 (6) (2024) 631–640.
- [11] S. Goswami, M. Yin, Y. Yu, G. E. Karniadakis, A physics-informed variational DeepONet for predicting crack path in quasi-brittle materials, *Computer Methods in Applied Mechanics and Engineering* 391 (2022) 114587.
- [12] T. Kurth, S. Subramanian, P. Harrington, J. Pathak, M. Mardani, D. Hall, A. Miele, K. Kashinath, A. Anandkumar, Fourcastnet: Accelerating global high-resolution weather forecasting using adaptive fourier neural operators, in: Proceedings of the platform for advanced scientific computing conference, 2023, pp. 1–11.
- [13] S. Karumuri, R. Tripathy, I. Bilionis, J. Panchal, Simulator-free solution of high-dimensional stochastic elliptic partial differential equations using deep neural networks, *Journal of Computational Physics* 404 (2020) 109120.
- [14] M. Abdar, F. Pourpanah, S. Hussain, D. Rezazadegan, L. Liu, M. Ghavamzadeh, P. Fieguth, X. Cao, A. Khosravi, U. R. Acharya, et al., A review of uncertainty quantification in deep learning: Techniques, applications and challenges, *Information fusion* 76 (2021) 243–297.
- [15] Z. Zou, X. Meng, A. F. Psaros, G. E. Karniadakis, Neuraluq: A comprehensive library for uncertainty quantification in neural differential equations and operators, *SIAM Review* 66 (1) (2024) 161–190.
- [16] Z. Zou, X. Meng, G. E. Karniadakis, Uncertainty quantification for noisy inputs–outputs in physics-informed neural networks and neural operators, *Computer Methods in Applied Mechanics and Engineering* 433 (2025) 117479.
- [17] S. Kaltenbach, P. Perdikaris, P.-S. Koutsourelakis, Semi-supervised invertible neural operators for bayesian inverse problems, *Computational Mechanics* 72 (3) (2023) 451–470.
- [18] R. Molinaro, Y. Yang, B. Engquist, S. Mishra, Neural inverse operators for solving pde inverse problems, arXiv preprint arXiv:2301.11167 (2023).

- [19] S. Karumuri, I. Bilionis, Learning to solve bayesian inverse problems: An amortized variational inference approach using gaussian and flow guides, *Journal of Computational Physics* 511 (2024) 113117.
- [20] D. Long, S. Zhe, Invertible fourier neural operators for tackling both forward and inverse problems, *arXiv preprint arXiv:2402.11722* (2024).
- [21] S. W. Cho, H. Son, Physics-informed deep inverse operator networks for solving pde inverse problems, *arXiv preprint arXiv:2412.03161* (2024).
- [22] V. Kag, D. R. Sarkar, B. Pal, S. Goswami, Learning hidden physics and system parameters with deep operator networks, *arXiv preprint arXiv:2412.05133* (2024).
- [23] K. Shukla, V. Oommen, A. Peyvan, M. Penwarden, N. Plewacki, L. Bravo, A. Ghoshal, R. M. Kirby, G. E. Karniadakis, Deep neural operators as accurate surrogates for shape optimization, *Engineering Applications of Artificial Intelligence* 129 (2024) 107615.
- [24] M. Ramezankhani, A. Deodhar, R. Y. Parekh, D. Birru, An advanced physics-informed neural operator for comprehensive design optimization of highly-nonlinear systems: An aerospace composites processing case study, *arXiv preprint arXiv:2406.14715* (2024).
- [25] J. Zhang, S. Zhang, G. Lin, Multiauto-deeponet: A multi-resolution autoencoder deeponet for nonlinear dimension reduction, uncertainty quantification and operator learning of forward and inverse stochastic problems, *arXiv preprint arXiv:2204.03193* (2022).
- [26] X. Yu, S. Hooten, Z. Liu, Y. Zhao, M. Fiorentino, T. Van Vaerenbergh, Z. Zhang, Seponet: Efficient large-scale physics-informed operator learning, in: *NeurIPS 2024 Workshop on Data-driven and Differentiable Simulations, Surrogates, and Solvers*.
- [27] L. Mandl, S. Goswami, L. Lambers, T. Ricken, Separable deeponet: Breaking the curse of dimensionality in physics-informed machine learning, *arXiv preprint arXiv:2407.15887* (2024).
- [28] P. Jin, S. Meng, L. Lu, Mionet: Learning multiple-input operators via tensor product, *SIAM Journal on Scientific Computing* 44 (6) (2022) A3490–A3514.
- [29] J. He, S. Koric, S. Kushwaha, J. Park, D. Abueidda, I. Jasiuk, Novel DeepONet architecture to predict stresses in elastoplastic structures with variable complex geometries and loads, *Computer Methods in Applied Mechanics and Engineering* 415 (2023) 116277.
- [30] K. Kontolati, S. Goswami, M. D. Shields, G. E. Karniadakis, On the influence of over-parameterization in manifold based surrogates and deep neural operators, *Journal of Computational Physics* 479 (2023) 112008.
- [31] Q. Cao, S. Goswami, T. Tripura, S. Chakraborty, G. E. Karniadakis, Deep neural operators can predict the real-time response of floating offshore structures under irregular waves, *Computers & Structures* 291 (2024) 107228.

- [32] V. Kumar, S. Goswami, K. Kontolati, M. D. Shields, G. E. Karniadakis, Synergistic Learning with Multi-Task DeepONet for Efficient PDE Problem Solving, arXiv preprint arXiv:2408.02198 (2024).
- [33] E. Haghigiat, U. bin Waheed, G. Karniadakis, En-deeponet: An enrichment approach for enhancing the expressivity of neural operators with applications to seismology, Computer Methods in Applied Mechanics and Engineering 420 (2024) 116681.
- [34] J. He, S. Kushwaha, J. Park, S. Koric, D. Abueidda, I. Jasiuk, Sequential deep operator networks (s-deeponet) for predicting full-field solutions under time-dependent loads, Engineering Applications of Artificial Intelligence 127 (2024) 107258.
- [35] S. Karumuri, L. Graham-Brady, S. Goswami, Efficient training of deep neural operator networks via randomized sampling, arXiv preprint arXiv:2409.13280 (2024).
- [36] K. Michałowska, S. Goswami, G. E. Karniadakis, S. Riemer-Sørensen, Neural operator learning for long-time integration in dynamical systems with recurrent neural networks, in: 2024 International Joint Conference on Neural Networks (IJCNN), IEEE, 2024, pp. 1–8.
- [37] M. L. Taccari, H. Wang, S. Goswami, M. De Florio, J. Nuttall, X. Chen, P. K. Jimack, Developing a cost-effective emulator for groundwater flow modeling using deep neural operators, Journal of Hydrology 630 (2024) 130551.
- [38] S. Qin, F. Lyu, W. Peng, D. Geng, J. Wang, N. Gao, X. Liu, L. L. Wang, Toward a better understanding of fourier neural operators: Analysis and improvement from a spectral perspective, arXiv preprint arXiv:2404.07200 (2024).
- [39] T. Tripura, S. Chakraborty, Wavelet neural operator for solving parametric partial differential equations in computational mechanics problems, Computer Methods in Applied Mechanics and Engineering 404 (2023) 115783.
- [40] S. Cai, Z. Wang, L. Lu, T. A. Zaki, G. E. Karniadakis, Deepm&mnet: Inferring the electroconvection multiphysics fields based on operator approximation by neural networks, Journal of Computational Physics 436 (2021) 110296.
- [41] C. Lin, Z. Li, L. Lu, S. Cai, M. Maxey, G. E. Karniadakis, Operator learning for predicting multiscale bubble growth dynamics, The Journal of Chemical Physics 154 (10) (2021).
- [42] Z. Mao, L. Lu, O. Marxen, T. A. Zaki, G. E. Karniadakis, Deepm&mnet for hypersonics: Predicting the coupled flow and finite-rate chemistry behind a normal shock using neural-network approximation of operators, Journal of computational physics 447 (2021) 110698.
- [43] B. Liu, N. Kovachki, Z. Li, K. Azizzadenesheli, A. Anandkumar, A. M. Stuart, K. Bhattacharya, A learning-based multiscale method and its application to inelastic impact problems, Journal of the Mechanics and Physics of Solids 158 (2022) 104668.

[44] P. C. Di Leoni, L. Lu, C. Meneveau, G. E. Karniadakis, T. A. Zaki, Neural operator prediction of linear instability waves in high-speed boundary layers, *Journal of Computational Physics* 474 (2023) 111793.

[45] Z. Jiang, M. Zhu, L. Lu, Fourier-mionet: Fourier-enhanced multiple-input neural operators for multiphase modeling of geological carbon sequestration, *Reliability Engineering & System Safety* 251 (2024) 110392.

[46] S.-T. Chiu, J. Hong, U. Braga-Neto, Deepsets: Non-autoregressive in-context learning of supervised learning operators, arXiv preprint arXiv:2410.09298 (2024).

[47] T. Wang, C. Wang, Latent neural operator for solving forward and inverse pde problems, arXiv preprint arXiv:2406.03923 (2024).

[48] T. Wang, C. Wang, Latent neural operator pretraining for solving time-dependent pdes, arXiv preprint arXiv:2410.20100 (2024).

[49] Q. Meng, Y. Li, Z. Deng, X. Liu, G. Chen, Q. Wu, C. Liu, X. Hao, A general reduced-order neural operator for spatio-temporal predictive learning on complex spatial domains, arXiv preprint arXiv:2409.05508 (2024).

[50] S. Wang, H. Wang, P. Perdikaris, Learning the solution operator of parametric partial differential equations with physics-informed DeepONets, *Science advances* 7 (40) (2021) eabi8605.

[51] S. Goswami, A. Bora, Y. Yu, G. E. Karniadakis, Physics-informed deep neural operator networks, in: *Machine Learning in Modeling and Simulation: Methods and Applications*, Springer, 2023, pp. 219–254.

[52] Z. Li, H. Zheng, N. Kovachki, D. Jin, H. Chen, B. Liu, K. Azizzadenesheli, A. Anandkumar, Physics-informed neural operator for learning partial differential equations, *ACM/JMS Journal of Data Science* 1 (3) (2024) 1–27.

[53] N. Navaneeth, T. Tripura, S. Chakraborty, Physics informed wno, *Computer Methods in Applied Mechanics and Engineering* 418 (2024) 116546.

[54] T. O’Leary-Roseberry, X. Du, A. Chaudhuri, J. R. Martins, K. Willcox, O. Ghattas, Learning high-dimensional parametric maps via reduced basis adaptive residual networks, *Computer Methods in Applied Mechanics and Engineering* 402 (2022) 115730.

[55] C. M. Bishop, N. M. Nasrabadi, *Pattern recognition and machine learning*, Vol. 4, Springer, 2006.

[56] K. Willcox, J. Peraire, Balanced model reduction via the proper orthogonal decomposition, *AIAA journal* 40 (11) (2002) 2323–2330.

[57] P. Benner, S. Gugercin, K. Willcox, A survey of projection-based model reduction methods for parametric dynamical systems, *SIAM review* 57 (4) (2015) 483–531.

- [58] F. Vetrano, F. Mastroddi, R. Ohayon, Pod approach for unsteady aerodynamic model updating, *CEAS Aeronautical Journal* 6 (2015) 121–136.
- [59] C. W. Rowley, Model reduction for fluids, using balanced proper orthogonal decomposition, *International Journal of Bifurcation and Chaos* 15 (03) (2005) 997–1013.
- [60] B. R. Noack, M. Morzynski, G. Tadmor, Reduced-order modelling for flow control, Vol. 528, Springer Science & Business Media, 2011.
- [61] A. Mohan, D. Daniel, M. Chertkov, D. Livescu, Compressed convolutional lstm: An efficient deep learning framework to model high fidelity 3d turbulence, *arXiv preprint arXiv:1903.00033* (2019).
- [62] X. Li, H. Bolandi, M. Masmoudi, T. Salem, A. Jha, N. Lajnef, V. N. Boddeti, Mechanics-informed autoencoder enables automated detection and localization of unforeseen structural damage, *Nature Communications* 15 (1) (2024) 9229.
- [63] J. A. Johnson, M. J. Heaton, W. F. Christensen, L. R. Warr, S. B. Rupper, Fusing climate data products using a spatially varying autoencoder, *Journal of Agricultural, Biological and Environmental Statistics* (2024) 1–14.

Appendix A. Appendix

Table A1: Summary of network architectures and hyperparameters used for training PI-Vanilla-NO model for the benchmarks considered. MLP refers to a multi-layer perceptron.

Case	Diffusion - reaction dynamics	Burgers' transport dynamics	Advection
Training and Test Configurations			
No. of input functions generated	2500	2500	2500
No. of testing trajectories (n_{test})	500	500	500
No. of training trajectories (n_{train})	{50, 100, 150, 200}	200	200
Discretization of the solution field $((n_t + 1) \times n_x)$	101×100	101×101	100×100
PI-Vanilla-NO Architectures and Training Settings			
DeepONet branch net	MLP: [100, 64, SiLU, 64, SiLU, 64, SiLU, 128]	MLP: [101, 64, SiLU, 64, SiLU, 64, SiLU, 128]	MLP: [100, 64, SiLU, 64, SiLU, 64, SiLU, 128]
DeepONet trunk net	MLP: [2, 64, SiLU, 64, SiLU, 64, SiLU, 128]	MLP: [2, 64, SiLU, 64, SiLU, 64, SiLU, 128]	MLP: [2, 64, SiLU, 64, SiLU, 64, SiLU, 128]
No. of input functions used per iteration (n_i)	64	64	64
No. of collocation points within the domain (n_t^r, n_x^r)	8, 8	8, 8	8, 8
No. of collocation points on each boundary (n_t^{bc}, n_x^{bc})	8, 1	8, 1	8, 1
No. of collocation points at $t = 0$ (n_x^{ic})	8	8	8
Constant learning rate	1e-3	1e-3	1e-3
No. of epochs	8000	8000	8000
Optimizer	Adam	Adam	Adam

Table A2: Summary of network architectures and hyperparameters used in our PI-Latent-NO model for the benchmarks considered. MLP refers to a multi-layer perceptron. PCA and Auto-encoder are used to reduce dimensionality.

Case	Diffusion - reaction dynamics	Burgers' transport dynamics	Advection
Training and Test Configurations			
No. of input functions generated	2500	2500	2500
No. of testing trajectories (n_{test})	500	500	500
No. of training trajectories (n_{train})	{50, 100, 150, 200}	200	200
Discretization of the solution field $((nt + 1) \times n_x)$	101×100	101×101	100×100
PCA Configurations			
Latent dimension size (d_z)	9	9	9
Variance Captured (%)	99.9%	99.9%	99.9%
Auto-encoder Architectures and Training Settings			
Latent dimension size (d_z)	9	9	9
Encoder net	MLP: $[n_x, 80, \text{SiLU}, 60, \text{SiLU}, 40, \text{SiLU}, d_z]$	MLP: $[n_x, 80, \text{SiLU}, 60, \text{SiLU}, 40, \text{SiLU}, d_z]$	MLP: $[n_x, 80, \text{SiLU}, 60, \text{SiLU}, 40, \text{SiLU}, d_z]$
Decoder net	MLP: $[d_z, 40, \text{SiLU}, 60, \text{SiLU}, 80, \text{SiLU}, n_x]$	MLP: $[d_z, 40, \text{SiLU}, 60, \text{SiLU}, 80, \text{SiLU}, n_x]$	MLP: $[d_z, 40, \text{SiLU}, 60, \text{SiLU}, 80, \text{SiLU}, n_x]$
Constant learning rate	$1e-3$	$1e-3$	$1e-3$
Batch size	64	64	64
No. of epochs	1000	1000	1000
Optimizer	Adam	Adam	Adam
Reconstruction error	$4.58e-5$	$1.77e-6$	$3.58e-6$
PI-Latent-NO Architectures and Training Settings			
Latent deepenet branch net	MLP: $[100, 64, \text{SiLU}, 64, \text{SiLU}, 64, \text{SiLU}, 16d_z]$	MLP: $[d_z, 64, \text{SiLU}, 64, \text{SiLU}, 64, \text{SiLU}, 16d_z]$	MLP: $[100, 64, \text{SiLU}, 64, \text{SiLU}, 64, \text{SiLU}, 16d_z]$
Latent deepenet trunk net	MLP: $[1, 64, \text{SiLU}, 64, \text{SiLU}, 64, \text{SiLU}, 16d_z]$	MLP: $[1, 64, \text{SiLU}, 64, \text{SiLU}, 64, \text{SiLU}, 16d_z]$	MLP: $[1, 64, \text{SiLU}, 64, \text{SiLU}, 64, \text{SiLU}, 16d_z]$
Reconstruction deepenet branch net	MLP: $[d_z, 64, \text{SiLU}, 64, \text{SiLU}, 64, \text{SiLU}, 128]$	MLP: $[d_z, 64, \text{SiLU}, 64, \text{SiLU}, 64, \text{SiLU}, 128]$	MLP: $[d_z, 64, \text{SiLU}, 64, \text{SiLU}, 64, \text{SiLU}, 128]$
Reconstruction deepenet trunk net	MLP: $[1, 64, \text{SiLU}, 64, \text{SiLU}, 64, \text{SiLU}, 128]$	MLP: $[1, 64, \text{SiLU}, 64, \text{SiLU}, 64, \text{SiLU}, 128]$	MLP: $[1, 64, \text{SiLU}, 64, \text{SiLU}, 64, \text{SiLU}, 128]$
No. of input functions used per iteration (n_i)	64	64	64
No. of collocation points within the domain (n_t^r, n_x^r)	8, 8	8, 8	8, 8
No. of collocation points on each boundary (n_t^{bc}, n_x^{bc})	8, 1	8, 1	8, 1
No. of collocation points at $t = 0$ (n_{ic}^{ic})	8	8	8
Constant learning rate	$1e-3$	$1e-3$	$1e-3$
No. of epochs	8000	8000	8000
Optimizer	Adam	Adam	Adam